Evaporation of moderately volatile elements from metal and sulfide melts: implications for volatile element abundances in magmatic iron meteorites

Article *in* Earth and Planetary Science Letters · September 2023

Edgar Steenstra
University of Münster

Christian Josef Renggli
University of Münster

Jasper Berndt
University of Münster

Contents lists available at ScienceDirect

Earth and Planetary Science Letters

journal homepage: www.elsevier.com/locate/epsl

Evaporation of moderately volatile elements from metal and sulfide melts: Implications for volatile element abundances in magmatic iron meteorites

E.S. Steenstra *, C.J. Renggli, J. Berndt, S. Klemme

Institute of Mineralogy, University of Münster, Germany

ARTICLE INFO

Article history:
Received 22 February 2023
Received in revised form 13 September 2023
Accepted 14 September 2023
Available online xxxx
Editor: F. Moynier

Keywords:
iron meteorite
moderately volatile elements
accretion
experimental petrology
evaporation

ABSTRACT

Volatile element abundances in magmatic iron meteorites provide fundamental insights into the processing of volatile elements in the early solar system. Although Cu, Ge and Ag concentrations of magmatic iron meteorites deviate up to 4 orders of magnitude between different magmatic iron meteorite groups, the role of evaporation on these volatile abundances is poorly constrained. Here, we experimentally assess the volatility of Cu, Ge, Ag, S, Cr, Co, Ni, Mo, Ru, Pd, W, Re and Ir from metal and sulfide melts as a function of pressure (10^{-4} and 1 bar), temperature (1573–1823 K) and time (5–120 min) for two end-member compositions (Fe versus FeS). These novel experiments demonstrate that the presence of S is a major parameter in establishing the volatility of Cu, Ge, Mo, Ag, Ru, W, Re and Ir. At constant *P-T* and time, the volatility of Ge, Mo, Ru, W, Re and Ir is greatly increased in the presence of S, whereas Cu and Ag are less volatile in the presence of S. At 1773 K and ∼0.001 bar, the volatility of S is sufficiently high that the degassed FeS liquid showed immiscibility of a S-rich sulfide and a S-poor Fe melt. Empirical equations were derived that predict the evaporative loss of Cu, Ge, Mo, Ag from Fe and/or FeS liquid as a function of temperature and time. A comparison of the newly derived volatility sequences with commonly applied 50% condensation temperature models shows that the condensation temperature models cannot be applied to sulfur-bearing Fe liquids and therefore to magmatic iron meteorites. Application of the new models on previously derived elemental depletions in the IVB parent body shows that evaporation, if it occurred, cannot have taken place under S-rich conditions. The latter would result in a depletion of Mo, which is not observed for the IVB irons. However, evaporation of a S-free or S-poor Fe liquid reproduces the observed volatility depletion trend for IVB irons under a wider range of temperature and evaporation times, demonstrating the potential importance of evaporative loss on the IVB parent body.

1. Introduction

The chemical composition of magmatic iron meteorites provides fundamental insights into planetary accretion processes, such as the architecture of the early solar system (carbonaceous (CC) versus noncarbonaceous (NC) magmatic iron meteorites; Rubin, 2018), core crystallization (Campbell and Humayun, 2005; Chabot and Zhang, 2021) and devolatilization processes (Kleine et al., 2018; Gargano and Sharp, 2019; Hirschmann et al., 2021). Magmatic iron meteorites are primarily distinguished based on their trace element compositions and potentially represent the cores of more than 50 parent bodies (Goldstein et al., 2009). The primary difference between the different groups is the degree of depletion in volatile elements, which increases from type I to IV iron meteorites (Scott and Wasson, 1975). The class of the IVB iron meteorites is thus one of the most volatile element-depleted meteorite suites. As nucleosynthetic isotope anomalies of IVB iron meteorites revealed that these meteorites are indeed members of the carbonaceous chondrite group (Budde et al., 2016), they must have accreted beyond the ice line and therefore may have been very rich in volatile and moderately volatile elements initially (Kruijer et al., 2017). However, similar bulk Ga and Ge concentrations of CC and NC magmatic iron meteorites do not suggest significantly different initial volatile contents of bulk CC and NC parent bodies (Rubin, 2018).

The exact processes (i.e., nebular versus at the time of accretion) responsible for the volatile loss in magmatic irons, including IVB´s, therefore remain uncertain. Depletions could have been in-

* Corresponding author.
E-mail address: esteenst@uni-muenster.de (E.S. Steenstra).

https://doi.org/10.1016/j.epsl.2023.118406
0012-821X/

herited from incorporation of chondritic precursor material (Sears, 1978; Wai and Wasson, 1979; Scott, 1979; Chen et al., 2013) and/or result from volatile loss during large impact events (Horan et al., 2012). Campbell and Humayun (2005) proposed that nebular processing controlled their abundances, based on the relative abundances of refractory siderophile elements in the IVB parent melt. On the other hand, Fe, Cr and W (but not Ni or Co) have been inferred to have been lost at $\sim \Delta IW = -1$ prior to fractional crystallization of the IVB melt (Rasmussen et al., 1984; Campbell and Humayun, 2005). Campbell and Humayun (2005) observed that elements with a condensation temperature below Fe are increasingly depleted in the IVB meteorites. Davis (2006) also concluded that Ge/Ni varies strongly for different magmatic iron meteorite classes, but with very limited intra-group variation. Given that Ge/Ni is hardly affected by core crystallization processes and Ni is non-volatile, Ge must have been lost due to volatility-related fractionation. Kleine et al. (2018) reported new Ag isotopic data for IVB´s that would be most consistent with loss of volatiles from a molten metallic core while exposed to space, after a catastrophic disruption of the parent body. Such volatile loss would also be consistent with previous models that suggested that the IVB parent body may have experienced internal temperatures exceeding 1760 K (Campbell and Humayun, 2005). It has been proposed that the IVA parent body core may also have experienced evaporative loss of Ag (Horan et al., 2012) due to impact disruption and removal of the mantle. Such an event is also suggested from the inverse correlation of metallographic cooling rates and Ni contents or degrees of fractional crystallization (Yang et al., 2007). Finally, it was concluded that evaporation of Ag from metallic melts is a viable model to account for Pd-Ag systematics of both the IVA (Matthes et al., 2018) and IVB cores (Kleine et al., 2018).

Copper is the most depleted element in the IVB suite, although Cu and $d^{65}Cu$ are not correlated (Bishop et al., 2012). Copper isotope data for most magmatic iron groups, including IVB's, also have strongly negative $\delta^{65}Cu$ values (i.e., down to $-2.26‰$), the opposite of what would be expected if Cu was predominantly lost through evaporation (Bishop et al., 2012; Chen et al., 2016). However, Chen et al. (2016) showed that the $\delta^{65}Cu$ data for the IVB suite are strongly modified by neutron capture, through the reaction $^{62}Ni(n,\gamma)^{63}Ni$ followed by beta decay to ^{63}Cu, and proposed an average pre-exposure value of $\delta^{65}Cu$ of $-0.3\pm0.8‰$, within the range of other iron meteorite groups and chondrites. Altogether, this could suggest that Cu was not lost due to volatility-related fractionation. This highlights the difficulties to ascribe mass-dependent processes unambiguously as Cu only has 2 isotopes, in conjunction with the aforementioned significant nucleosynthetic variations among chondrites (Luck et al., 2003, 2005). Finally, it could reflect initial extensive evaporation, followed by partial recondensation of Cu in the kinetic regime, as proposed for K in angrites (Hu et al., 2022). Tungsten and Cr may have been lost early (Rasmussen et al., 1984; Campbell and Humayun, 2005), consistent with the observed anomalous behavior of W compared to Mo in magmatic iron meteorites, as they are expected to exhibit similar geochemical behavior (Scott, 1978).

Volatile loss may have been significant for S, as it is commonly assumed to be more volatile than Cu, at least during condensation from a highly reduced solar gas at 10^{-4} bar (e.g., Wood et al., 2019). Previous studies showed that iron meteorites typically contain bulk S contents of approximately 0 to 2 wt.% (Buchwald, 1975). However, it is believed that many magmatic iron meteorite parent bodies were potentially far richer in S (up to 10% bulk core S; Chabot and Zhang, 2021) and that samples of S-rich portions were perhaps selectively destroyed (Hirschmann et al., 2021 and references therein). Depending of the difference in volatility of elements for S-bearing and S-free metal alloys, depletions of such elements may be used to investigate the timing of S loss from magmatic iron meteorites. To investigate the nature of volatile element depletions in magmatic iron meteorites, novel degassing experiments were conducted to systematically quantify the (potential) evaporative loss of Cr, Cu, Ge, Ag and W from metal and sulfide melts. Several other, nominally non-volatile elements (Co, Ni, Mo, Ru, Pd, Re and Ir) were added to assess their volatility in S-free and S-rich metal melts.

2. Methods

2.1. Experimental

Metal and sulfide mixtures were melted in a gas mixing furnace at the Institute of Mineralogy, University of Münster. Experiments were conducted at both 1 bar and at low vacuum (∼0.0007–0.0013 bar) for variable run times (5–120 min). Peak temperatures of 1573–1823 K were explored and correspond with peak thermal conditions typically inferred for asteroidal differentiation processes (e.g., Campbell and Humayun, 2005). Experiments run at 1 bar were flushed with pure CO and buffered the experiments with the graphite buckets at the graphite – CO (GCO) buffer. Temperatures were monitored and controlled using a type B thermocouple and a Eurotherm 3508 programmable controller. The estimated temperature uncertainties are less than 5 degrees. Vacuum was attained in the furnace by attaching an Alcatel vacuum pump to the lower end of the vertical furnace tube (alumina) and sealing the gas-input valve at the top of the furnace. The pressure was monitored with an Edwards vacuum gauge controller. The vacuum experiments were conducted by first ramping the furnace up to the target temperature, without any sample present. The sample hanger and sample were then hung in the top section of the furnace, far away from the hotspot, and the furnace was subsequently depressurized. When the target pressure was reached, the sample holder and sample were rapidly lowered into the hot spot.

Starting compositions consisted of high-purity FeS or Fe powders doped with 0.1 mol% of high-purity Cr, Co, Ni, Cu, Ge, Mo, Ru, Pd, Ag, W, Re and Ir powders. Two end-member starting compositions (Fe + traces, FeS + traces) were chosen to explore the effects of S on the volatility of the elements of interest. Mixtures were mixed in an agate mortar under ethanol for at least 30 min to ensure homogeneous starting compositions. Trace-element doped sulfide and metal powders were loaded in separate, ∼2 cm long graphite buckets (∼4−5 mm O.D., ∼3 mm I.D.) that in turn were placed in a larger single graphite bucket of ∼4–5 cm long and 2–3 cm wide. The graphite buckets were suspended by Pt or Re wire depending of the experimental conditions. The graphite capsules were filled to approximately 2/3 of their length by using pins to ensure proper packing of the starting mixtures. Although the use of graphite buckets inevitably results in the presence of C in Fe and to a lesser extent FeS liquid, graphite was found to be the most convenient bucket material due to its high melting point, limited weight and softness allowing for simple machining. Runs performed with FeS powders under vacuum were initially challenging due to the consistent loss of the FeS powder charge from the graphite capsule at the onset of depressurizing, despite careful and tight packing of the powder in the capsule. Post-experimental investigation showed that these mixtures were only sintered and not quenched, suggesting run products were rapidly lost from the hotspot in the first few seconds of the experiment. This issue was addressed by drilling a small hole (0.5–1.5 mm diameter) in the bottom of the graphite capsule in conjunction with pressing of the FeS powder into a dense pellet at room temperature. Using this approach, such vacuum-driven losses were subsequently largely prevented. However, preferably a solid starting material is used rather than a powder. This is because there are potential time lag effects associated with the melting of a powder (Sossi et al., 2019),

relative to the use of a solid material, potentially yielding an overestimation of the time during which a melt can effectively degas. However, the melting of the starting materials of interest would inevitably result in large elemental losses due to its very low viscosity in conjunction with the expected volatility of the elements of interest. Therefore, powdered starting materials were used for all experiments.

After the experiments, the retrieved run products were mounted in epoxy resin and polished using various grades of SiC sandpaper and polycrystalline diamond spray. The samples were carbon-coated for imaging and chemical analyses of major elements by electron microprobe, after which they were analyzed for trace elements by LA-ICP-MS.

2.2. Analytical

Experimental run products were imaged and analyzed for major (Fe, S, O) and minor/trace element (Cr, Mn, Ni, W, Re, Ir) contents using the JEOL JXA 8530F electron microprobe at the University of Münster (Tables S.1, S.2). Phases were analyzed using a defocused beam (2–20 µm), depending on available surface area, with beam currents of 15–20 nA and an accelerating voltage of 15 kV. Measurement points were set in lines and/or raster grids. Special care was taken to avoid analyses of areas close to the edge of phases and/or surrounding capsule materials. Counting times were 10–30 s on peak and 5–15 seconds on each background. Analyses for sulfide liquids and silicate melts were calibrated on well-characterized natural and synthetic micro-analytical reference materials. Standards used for metal and sulfide analyses were pyrite for Fe and S, MgO for O, and pure metal standards for Ti, Mn, Cr, Ni, W, Re, Ir. The reader is referred to Steenstra et al. (2020) for additional details on the electron microprobe analyses which were obtained using the same procedure. Trace elements were determined using nanosecond-laser ablation inductively coupled plasma mass spectrometry (ns-LA-ICP-MS). All LA-ICP-MS analyses were performed using a 193 nm ArF excimer laser (Analyte G2, Photon Machines) connected to an Element XR mass spectrometer. Repetition rate was set to 10 Hz at an energy of ∼3–4 J/cm^2 throughout the entire session and beam sizes ranging between 25–110 µm. The preferred and most commonly used beam size throughout the study was 110 µm, but in case of Fe alloy blobs in sulfide liquids beam sizes were in some cases reduced. The following masses were monitored in low resolution mode: ^{24}Mg, ^{27}Al, ^{29}Si, ^{43}Ca, ^{49}Ti, ^{51}V, ^{53}Cr, ^{55}Mn, ^{56}Fe, ^{59}Co, ^{60}Ni, ^{61}Ni, ^{63}Cu, ^{65}Cu, ^{66}Zn, ^{71}Ga, ^{73}Ge, ^{75}As, ^{77}Se, ^{95}Mo, ^{101}Ru, ^{105}Pd, ^{107}Ag, ^{111}Cd, ^{115}In, ^{118}Sn, ^{121}Sb, ^{125}Te, ^{182}W, ^{185}Re, ^{193}Ir, ^{205}Tl, ^{208}Pb and ^{209}Bi. Mass windows were set to 10% measuring 100 samples/peak using a segment duration of 20 ms. The blank signal has been analyzed for 20 s and the peak signal for 40 s. The washout time was set to 10 s. Representative reference materials appropriate for Fe and FeS solids, containing comparable amounts of C and the elements of interest, are not available. We instead synthesized the various starting materials in a piston cylinder press at 1.5 GPa and 1773–1873 K in graphite capsules. At such high pressures, no degassing is expected for any of the elements of interest and comparable C contents of the quenched metal- and sulfide liquids are obtained. For example, an average of 14 experiments conducted at 1 bar yields an average estimated C content of 6.24±0.21 (2SE) wt.% and 11 experiments conducted at vacuum conditions yields an average C content of 6.49±0.39 (2SE) wt.%, the latter based on the difference between the EPMA totals and 100% (Fig. S.2). This value is in excellent agreement with the C content of the high pressure synthesized Fe starting materials of 6.59±0.33 (2SD) wt.% and close to and/or within the range of the predicted solubility of C in liquid Fe at 1 atmosphere within the temperature range of interest (5.87±0.52 at 1673–1873 K; Steenstra et al., 2020).

In all of the analyses, except for ^{101}Ru and ^{193}Ir, the NIST 610 glass was used as an external reference material for both high-pressure synthesized starting materials and experimental run products (Jochum et al., 2005a). The use of the non-matrix-matched NIST 610 glass for quantification of absolute elemental concentrations in FeS- and Fe-based samples will certainly yield significant matrix effects, particularly for nominally volatile and refractory elements such as Ge, Ir, W, Re (Steenstra et al., 2019, 2020; Fig. S.3). The high-pressure synthesized metals and sulfides have a (near)-identical composition to the degassed samples in terms of major elements (Fe, S). Given that the reported evaporative loss factors are defined simply as ratios relative to the high *P-T* starting material, any matrix effects arising from the use of non-matrix matched reference materials would thus be effectively canceled out. For quantification of ^{101}Ru and ^{193}Ir abundances, a Cu and/or Ni sulfide (Wohlgemuth-Ueberwasser et al., 2007) and the GSD-1G glass (Jochum et al., 2005b) was used, respectively. The Fe abundances (assuming ^{56}Fe) of metals and sulfides as measured by electron microprobe were used as internal standards in all analyses. The LA-ICP-MS data was reduced using GLITTER software (van Achterbergh et al., 2001; Griffin et al., 2008) and included monitoring and/or identification of heterogeneities or potential spatial compositional variations in the exposed section through the run products.

3. Results

3.1. Run products

Run products were generally characterized by a single quenched metal or sulfide blob embedded within the graphite bucket (Fig. 1). Although texture types varied greatly between run products obtained at different temperatures (Fig. 1), all samples showed textures indicative of metals and sulfides being fully molten at the time of quenching. This is consistent with phase diagrams that predict that C-saturated Fe liquid and FeS liquid are fully molten above ∼1545 K and 1420 K at ambient pressures, respectively (Lord et al., 2009; Buono and Walker, 2011, and references therein). Quenched metal liquids show small graphite inclusions throughout the samples (Fig. 1a-c), in agreement with a C-saturated state of the metallic liquid. Carbon concentrations were not directly measured but can be roughly assessed for Fe liquid experiments by consideration of the EPMA totals (Table S.2).

Some of the sulfide liquids degassed under vacuum experienced extensive loss of S, resulting in the immiscibility of a S-poor, C-rich Fe liquid and a S-rich, C-poor FeS melt (Fig. 1e; Table 1), consistent with previously derived phase equilibria predictions (Corgne et al., 2008). In the runs conducted over the longest run times (120 min) at 1773 K almost all S degassed (Table 1). The FeS samples also often contain tiny (<10 µm) Ru-, W-, Re- and/or Ir-rich blebs, which contain almost the bulk inventory of the latter elements (see also next section). The formation of the latter blebs is a direct result of their low solubility in FeS matte (Fonseca et al., 2007, 2011). To obtain representative bulk compositions of the samples that contained either immiscible C- and S-rich molten alloy or PGE-rich nuggets, modal analyses were performed by using the backscattered electron images of the experiments in conjunction with image processing software Image Color Extract Tool®. The bulk compositions of the samples were then calculated by using the measured compositions of the different phases with the derived modal abundances of the phases (Table S.2). Finally, some disagreement is observed between the expected starting mix composition and the measured starting composition synthesized at high *P-T* (e.g., W). This is most likely the result of complex matrix effects arising from using the non-matrix-matched NIST-610 glass for the LA-ICP-MS analyses of metal and sulfide matrices

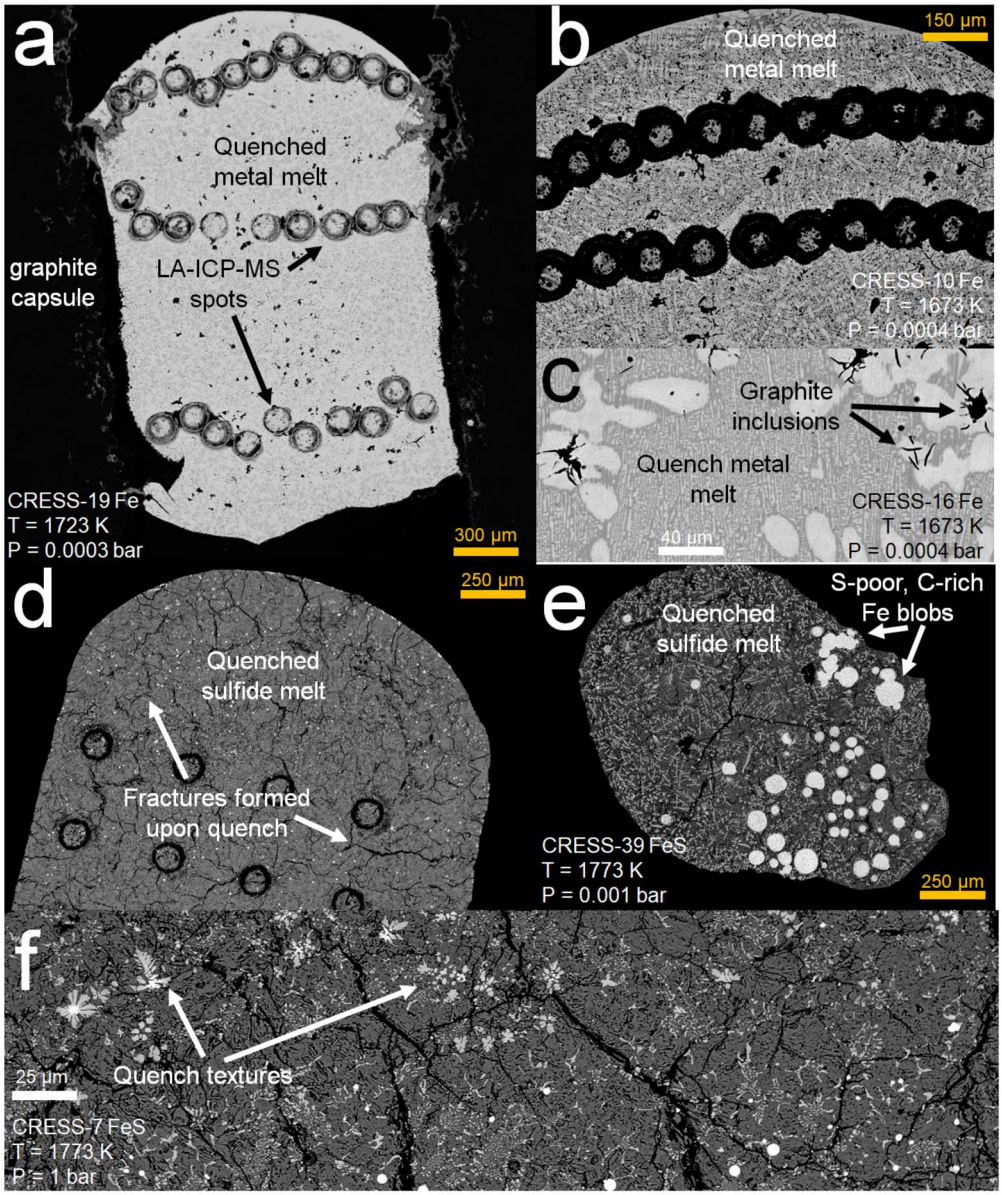

Fig. 1. Backscattered electron images of typical experimental run products. Panels **a-c** depict run products for Fe melts, showing a variety of quench textures (**b, c**) with abundant graphite inclusions. Pits are LA-ICP-MS spots placed in horizontal and/or vertical transects. Panels **d-f** show run products using a FeS starting composition, with typical cracks formed during quenching and other quench textures. Panel ***e*** shows experiments CRESS-39, in which S degassing was sufficiently high to result in immiscibility of a S-poor, C-rich and S-rich, C-poor Fe liquid.

(e.g., Steenstra et al., 2019, 2020) and/or small uncertainties in the weighing of the starting mixtures. However, given that the experimental samples are normalized relative to the high *P-T* synthesized starting composition, matrix effects and/or weighing errors do not affect the presented results.

3.2. Homogeneity of quenched metal and sulfide liquids

Metal and/or sulfide liquids may be heterogeneous if degassing of the elements of interest is diffusion-limited within the liquid. To assess the potential of heterogeneous distribution of trace elements in the experimental quenched liquids, LA-ICP-MS spots were placed in horizontal and/or vertical raster lines (Fig. 2). Only very limited variation of measured element contents between very different areas of the samples is generally observed. This suggests that the very low viscosities of both the sulfide and metal melts are sufficient for maintaining a homogeneous distribution of trace elements throughout the melts despite evaporation. A notable exception is the large variation in Ru, W, Re, Ir abundances in sulfide melts, especially at lower temperatures, which is instead due to the presence of nuggets due to their oversaturation in FeS liquid as previously discussed. It should be noted that these nuggets are minor in abundance (<0.83 modal %) and do not contain significant amounts of Ni and other elements of interest, thereby not affecting the results for the other elements of interest (e.g., Cu, Ge, Mo, Ag).

Post-experimental results showed that some Fe liquid experiments that were conducted at 1 bar together with FeS melts – although at a distance and isolated in tall graphite buckets - suffered from some S cross-contamination (Fig. S.4). No other elemental cross-contamination was observed. An increase of S contents relative to starting compositions was only found to be significant for experiments CRESS-5 to 8 Fe, and CRESS-26 Fe, 27 Fe, 32 Fe and 38 Fe, with post-experimental S abundances of up to 0.76 wt.%, but usually much less (<0.30 wt.) (Table S.1).

Table 1
Experimental run conditions.

	T (K)	P (bar)	Time (min)	Starting comp[a]	Observed phases[b]	$\log f^{(S/Ni)}$	Comments
CRESS-5 Fe	1673	1	15	Fe A	Fe	–	Performed together with CRESS-5 FeS
CRESS-5 FeS	1673	1	15	FeS A	FeS, Fe-W-Re-Ir alloy	−0.06(5)	Performed together with CRESS-5 Fe
CRESS-6 Fe	1773	1	15	Fe A	Fe	–	Performed together with CRESS-6 FeS
CRESS-6 FeS	1773	1	15	FeS A	FeS, Fe-W-Re-Ir alloy	−0.02(3)	Performed together with CRESS-6 Fe
CRESS-7 Fe	1773	1	60	Fe A	Fe	–	Performed together with CRESS-7 FeS
CRESS-7 FeS	1773	1	60	FeS A	FeS, Fe-W-Re-Ir alloy	−0.04(3)	Performed together with CRESS-7 Fe
CRESS-8 Fe	1823	1	15	Fe A	Fe	–	Performed together with CRESS-8 FeS
CRESS-8 FeS	1823	1	15	FeS A	FeS, Fe-W-Re-Ir alloy	−0.05(5)	Performed together with CRESS-8 Fe
CRESS-10 Fe	1673	0.0004	15	Fe A	Fe	–	CRESS-10 FeS lost prior to melting[c]
CRESS-12 Fe	1773	0.0004	15	Fe A	Fe	–	CRESS-12 FeS lost prior to melting
CRESS-14 Fe	1573	0.0004	15	Fe A	Fe	–	CRESS-14 FeS lost prior to melting
CRESS-15 Fe	1623	0.0004	15	Fe A	Fe	–	CRESS-15 FeS lost prior to melting
CRESS-16 Fe	1673	0.0004	15	Fe A	Fe	–	CRESS-16 FeS lost prior to melting
CRESS-18 Fe	1673	0.0004	120	Fe A	Fe	–	CRESS-18 FeS lost prior to melting
CRESS-19 Fe	1723	0.0003	15	Fe A	Fe	–	CRESS-19 FeS lost prior to melting
CRESS-23 Fe	1573	0.0004	15	Fe A	Fe	–	CRESS-23 FeS lost prior to melting
CRESS-24 FeS	1573	0.0004	15	FeS A	FeS, Fe-Ru-W-Re-Ir alloy	−0.07(9)	–
CRESS-25 Fe	1623	0.0004	15	Fe A	Fe	–	CRESS-25 FeS lost prior to melting
CRESS-26 Fe	1773	1	5	Fe A	Fe	–	Performed together with CRESS-26 FeS
CRESS-26 FeS	1773	1	5	FeS A	FeS, Fe-W-Re-Ir alloy	−0.02(3)	Performed together with CRESS-26 Fe
CRESS-27 Fe	1773	1	30	Fe A	Fe	–	Performed together with CRESS-27 FeS
CRESS-27 FeS	1773	1	30	FeS A	FeS, Fe-W-Re-Ir alloy	−0.03(3)	Performed together with CRESS-27 Fe
CRESS-32 Fe	1773	1	120	Fe A	Fe	–	Performed together with CRESS-32 FeS
CRESS-32 FeS	1773	1	120	FeS A	FeS, Fe-Ru-W-Re alloy	−0.04(3)	Performed together with CRESS-32 Fe
CRESS-33-FeS	1573	1	15	FeS A	FeS, Fe-W-Re-Ir alloy	0.00(3)	–
CRESS-34 FeS	1623	0.0013	15	FeS A	FeS, Fe-Ru-W-Re-Ir alloy	−0.06(5)	–
CRESS-35 FeS	1673	0.0010	15	FeS A	FeS, Fe-Ru-W-Re-Ir alloy	−0.09(2)	–
CRESS-36 FeS	1723	0.0010	15	FeS A	FeS, S-poor Fe-rich alloy	−0.11(2)	–
CRESS-37 FeS	1773	0.0010	5	FeS A,	FeS, S-poor Fe-rich alloy	−0.13(6)	CRESS-37 Fe lost prior to melting
CRESS-38 Fe	1773	0.0010	30	Fe A	Fe	–	CRESS-38 FeS lost prior to melting
CRESS-39 FeS	1773	0.0010	15	FeS A	FeS, S-poor Fe-rich alloy	−0.15(4)	–
CRESS-40 Fe	1773	0.0009	120	Fe A	Fe	–	CRESS-40 FeS lost prior to melting
CRESS-42 Fe	1773	0.0010	60	Fe A	Fe	–	CRESS-42 FeS lost prior to melting
CRESS-44 Fe	1773	0.0010	5	Fe A	Fe	–	–
CRESS-46 FeS	1773	0.0010	60	FeS A	S-poor Fe-rich alloy	−1.99(22)	Significant S loss
ESS-1-130-CR1 FeS	1573	1	15	FeS	FeS, Fe-W-Re-Ir alloy	−0.02(10)	–
ESS-1-150A1 Fe	1773	1	15	Fe A	Fe	–	–
ESS-1-150C1 Fe	1773	1	10	Fe A	Fe	–	–
ESS-1-150D1 FeS	1773	1	30	FeS A	FeS, Fe-W-Re-Ir alloy	−0.02(7)	–
ESS-V-140-CR1 FeS	1673	0.0003	15	FeS A	FeS, S-poor Fe-rich + Fe-W-Re-Ir alloy	−0.15(11)	–
ESS-V-140-CR2 FeS	1673	0.0003	31.5	FeS A	FeS, S-poor Fe-rich alloy	−0.47(15)	–
ESS-V-140-CR3 FeS	1673	0.0003	60	FeS A	FeS, S-poor Fe-rich + Fe-W-Re-Ir alloy	−0.44(10)	–
ESS-V-140-CR4 FeS	1673	0.0003	120	FeS A	FeS, S-poor Fe-rich alloy	−1.00(138)	–
NESS-1-135CR1-Fe	1623	1	15	Fe B	Fe	–	–
NESS-1-135CR1-FeS	1623	1	15	FeS B	FeS, Fe-W-Re alloy	0.02(5)	–
NESS-1-145CR1-Fe	1723	1	15	Fe B	Fe	–	–
NESS-1-145CR1-FeS	1723	1	15	FeS B	FeS	−0.01(4)	–
NESS-1-150CR1 Fe	1773	1	5	Fe B	Fe	–	–
NESS-1-150CR2 Fe	1773	1	15	Fe B	Fe	–	–
NESS-1-150CR3 Fe	1773	1	90	Fe B	Fe	–	–

[a] FeS A = FeS + 0.1 mole % of Cr, Co, Ni, Cu, Ge, Mo, Ru, Pd, Ag, W, Re and Ir; Fe A = Fe + 0.1 mole % Cr, Co, Ni, Cu, Ge, Mo, Ru, Pd, Ag, W, Re, Ir; FeS B = FeS + 0.1 mole % of Ni, Cu, Ge, Mo, Ag, W, Re; Fe B = Fe + 0.1 mole% of Ni, Cu, Ge, Ag. [b] FeS = quenched FeS liquid; Fe = quenched Fe liquid; S-poor Fe-rich alloy = immiscible S-poor quenched Fe liquid. Note: PGE-rich alloys were generally very small (<10 um). [c] Early loss of experiments prior to melting occurred due to escape of the sample during initial depressurization.

3.3. *Effect of high-temperature degassing on elemental abundances*

3.3.1. *Quantification of evaporative loss*

The potential evaporative loss of element i was quantified by considering the ratio between the concentration of element i in the reference material and the experimental sample, respectively:

$$\text{Evaporative loss factor of element } i\left(f^{i}\right) = \frac{\text{concentration of element } i \text{ in experimental sample (ppm)}}{\text{concentration of element } i \text{ in reference material (ppm)}} \quad (1)$$

The evaporative loss factors from Eq. (1) were then normalized to Ni:

$$\text{Ni – normalized evaporative loss factor of element i } f^{(i/Ni)} = \frac{f^{i}}{f^{Ni}} \quad (2)$$

The main reason for using Ni as a reference is that it is highly homogeneously distributed throughout the experiments, for both Fe and FeS liquids (Fig. 2). Nickel is also a major element in magmatic iron meteorites (Scott and Wasson, 1975). However, the above approach assumes that Ni behaves non-volatile at the experimental conditions of interest. This can be tested by comparing the behavior of a nominally highly refractory element such as Ir with Ni. Consideration of the Ir/Ni ratio shows no systematic variation, i.e., no increase of the Ir/Ni ratio with run time, pressure or temperature, suggesting Ni is not volatile under the experimental conditions explored here (see also sections 3.3.2 and 3.3.3.). Absolute

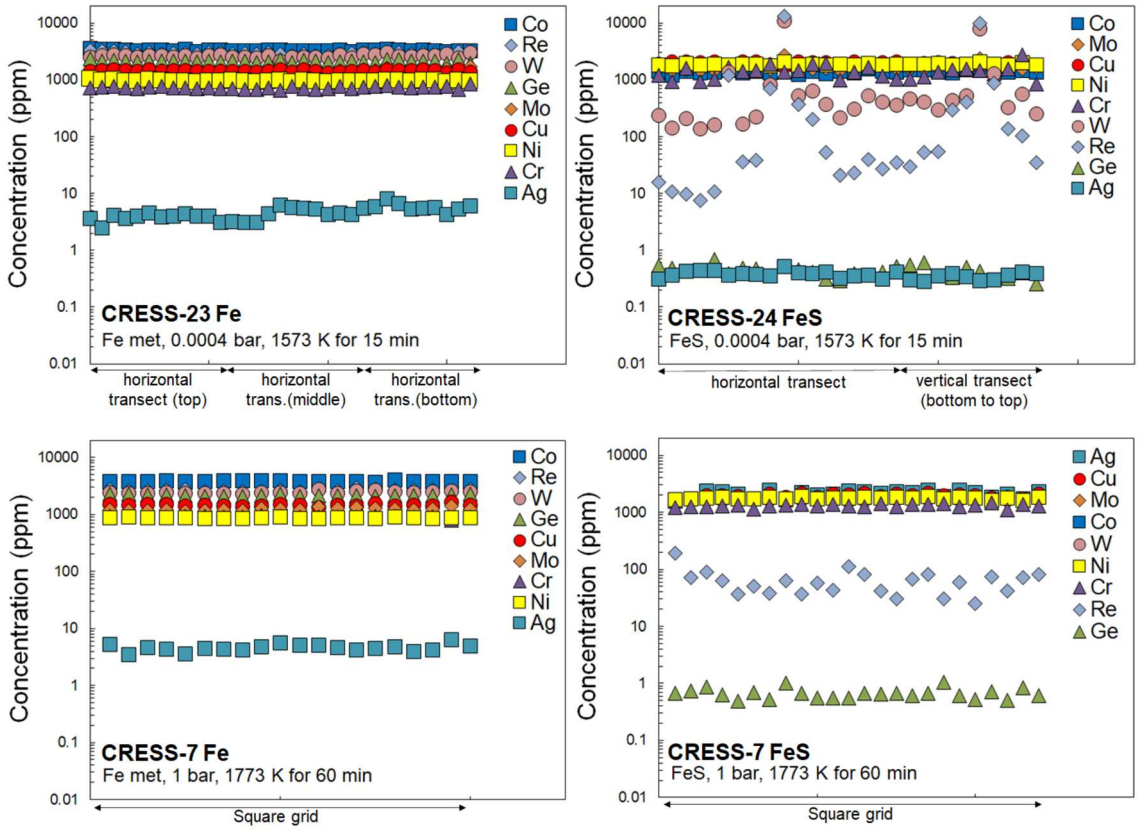

Fig. 2. Variability of measured volatile concentrations along horizontal and vertical LA-ICP-MS and/or grid spot transects on experimental run products CRESS 23 (Fe), CRESS 24 (FeS) and CRESS 7 (FeS, Fe). No significant systematic variability in elemental concentrations is observed throughout the samples. The relatively large variability in W and Re concentrations in FeS liquid is due to their low solubility in FeS liquid, resulting in the formation of (Ru)-W-Re-Ir rich phases (see text for detailed discussion). Uncertainties on individual spots are smaller than symbol sizes in all cases.

concentrations of Ni are also similar or deviate positively from the measured Ni content of the high *P-T* synthesized starting materials (up to +1800 ppm for FeS liquids and +700–800 ppm for Fe melts, Fig. S.5), confirming that Ni was not lost but rather enriched through preferential evaporation of Fe and/or S. Evaporative loss factors were predominantly based on LA-ICP-MS derived measurements, except for S and for experiments containing Ru-, W-, Re- and/or Ir-bearing HSE nuggets that were too small to be measured by LA-ICP-MS. For S and the latter experiments evaporative loss factors were based on EPMA measurements. Figs. 3, 4 and S.6 to S.18 show the logarithmic evaporative loss factors for all of the elements of interest (Table S.4; Appendix section A.2).

3.3.2. FeS liquid experiments

Analyses of the FeS liquids degassed at 1 bar show no evidence of volatile loss up to 1823 K for S, Fe, Cr, Co, Ni, Cu, and Pd (Fig. 3, Table S.4; Fig. S.6 to S.11). However, Ge, Mo and Ag and most likely Ru, Re, W and Ir are affected by volatility-related loss at these conditions (Fig. 3, Table S.4). Results for FeS melts degassed under vacuum at ∼0.001 bar imply, that the elements S, Cu, Ge, Mo, Ag are all evaporated at 1773 K (Fig. 3, 4), as well as Ru, Re, W and Ir (Table S.4, Fig. S.6 to S.12). The decrease of elemental volatility with increasing total pressure is discussed at length in previous studies (e.g., Richter et al., 2011; Sossi et al., 2020). It is a result of a shorter mean free patch (i.e., slower diffusion) of the evaporating species at ambient pressure, relative to vacuum, therefore yielding lower evaporation rates at ambient pressure. Elements Ru, Re, W and Ir are virtually in all experimental samples depleted by up to several orders of magnitude. However, the *P-T*-time dependencies are difficult to derive within the present study due to their low solubility in FeS matte and the resulting heterogeneous distribution.

3.3.3. Fe liquid experiments

Post-experimental analyses of the Fe liquids degassed at room pressure show that only Ag was lost considerably (up to 99.99%) within the studied temperature range (1673–1823 K) (Table S.4, Fig. 4; Fig. S.13 to S.18). Under the investigated redox conditions (∼CCO buffer), post-experimentally measured abundances of Cr, Co, Ni, Cu, Ge, Mo, Ru, Pd, W, Re and Ir suggest no loss of these elements at temperatures of up to 1823 K at 1 bar (Fig. 4, Table S.4, Fig. S.13 to S.18). Decreasing the pressure from 1 bar to ∼0.001 bar increases the volatility of Cu, Ge, Ag at 1673–1773 K resulting in $f^{(i/Ni)}$ values that are up to 5 orders of magnitude lower relative to the starting compositions. However, the other elements considered do not evaporate at these conditions (Fig. 3, Table S.4, Appendix section A.2).

3.3.4. The effect of S and C on elemental volatility in metallic melts

Comparing the results for Fe and FeS liquid shows that the presence of S greatly affects the volatility of Cu, Ge, Mo, Ru, Ag, W, Re and Ir (Table S.4, Fig. 3). In case of Ge, Mo, Ru, W, Re and Ir, the volatility is significantly increased by the addition of S at a given set of *P-T*-time conditions, whereas for Ag and Cu it is strongly decreased. It should be noted that the importance of S on Ge volatility was already suggested from previous thermodynamic calculations and volatility experiments relevant to silicate melts and fumarolic systems (Sears, 1978; Wai and Wasson, 1979; Renggli and Klemme, 2020). Generally, nominally sulfide-loving (chalcophile) elements such as Ag and Cu are observed to be less volatile in FeS liquid, compared to Fe liquid. This can be explained

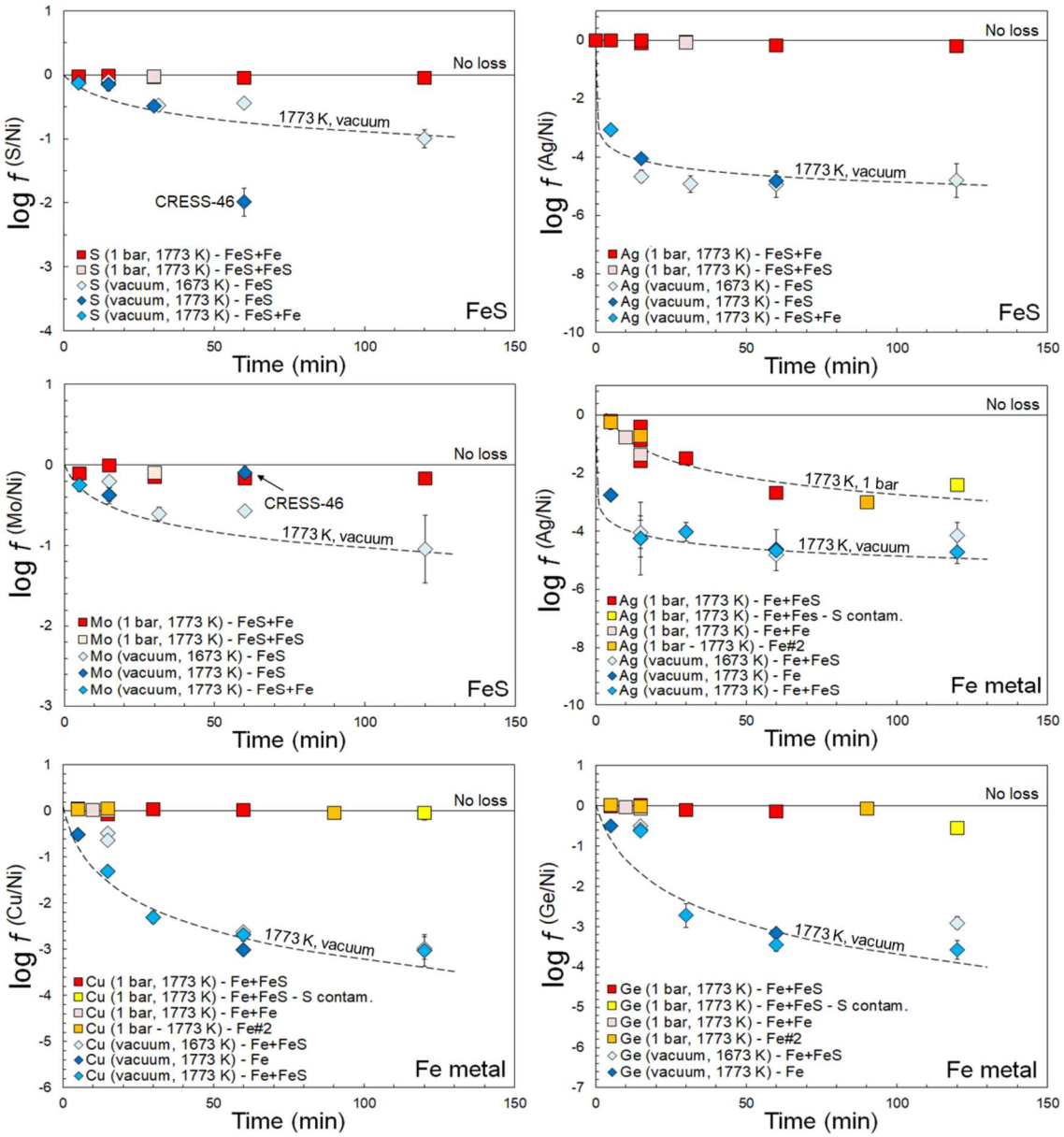

Fig. 3. Evaporative loss factors, normalized to Ni (Eq. (1), (2)), versus time for FeS and Fe liquids. Yellow stars and solid lines indicate the initial ratio prior to degassing. Reported uncertainties are based on maximum errors on LA-ICP-MS measured abundances in the high-pressure melted starting mixture and on experimental run products. Also shown (where available) are the modeled dependencies from Table 2. The data labels indicate whether the experiment was conducted simultaneously with a Fe or FeS run or if it was performed without another experiment present. The label #2 indicates the use of the second starting composition NESS FeS or Fe.

by the high activity coefficients of these elements in Fe liquid (e.g., Swartzendruber, 1984; Wood et al., 2014; Norris, 2017 and references therein), increasing their evaporative potential. On the other hand, nominally iron-loving (siderophile) elements such as Ge and Mo have high activity coefficients in FeS liquid (Wood et al., 2014; Norris, 2017 and references therein), promoting their evaporation from FeS liquid relative to Fe liquid. The strong effect of S on element volatilities is also evident from the experimental samples that experienced minor S cross-contamination or significant S loss (see discussion in section 3.2 and Fig. S.4). For example, Ge behaves significantly more volatile in run CRESS-32 Fe, that suffered from 0.75 wt.% S cross-contamination, compared to the expected trend of uncontaminated S-free Fe liquid evaporation experiments (Table S.4, Fig. S.14). On the other hand, chalcophile element Ag behaves less volatile in the presence of S, again consistent with the higher-than-expected Ag evaporative loss factor derived for experiment CRESS-32 Fe (Table S.4, Fig. S.16). Elements Mo, W and Re are volatile in S-contaminated run CRESS-38 Fe, whereas in nominally S-free experiments they are not (Table S.4). Sample CRESS-46 suffered significantly more S loss relative to experiments performed at comparable *P-T*-time conditions, resulting in more volatile behavior of Cu and less volatile behavior of Mo, Ru, W, Re and Ir (Fig. 3, Table S.4). The presence of S is therefore a key parameter in establishing the volatilities of Cu, Ge, Ag, Mo, Ru, W, Re and Ir.

Carbon, inevitably present due to the use of graphite buckets and/or a CO furnace atmosphere, may also affect the volatility of the elements of interest. However, all experiments were conducted in graphite buckets and the effects of C can therefore not be isolated at this point. However, given the observed systematics of elemental volatility for Fe and FeS melts that qualitatively reflect their activity coefficients in Fe and FeS melt, it is likely that the volatility of carbon-loving elements is decreased in C-saturated Fe liquid and vice-versa. Elements W and Mo are both carbon-loving (Siebert et al., 2011) and are expected to be more volatile in C-

Table 2
Summary of the parameterizations describing elemental volatility for FeS and Fe liquids and the fit parameters for temperature, time (t). The fits were obtained for (1) all data or (2) all data excluding plateau values which do not vary with experimental run time. The last column lists the lag time (t_0) correction parameters, where applicable.

Log	A	B (1/T (K))	C (log (experimental run time in min))	*N*	R^2	Lag time (t_0) in min
All data						
S/Ni (FeS) – vacuum	−1.286(1093)	3310(1874)	−0.725(116)	11	0.83	$7701e^{-0.00402053 * T(K)}$
Cu/Ni (FeS) – vacuum	1.496(4820)	n.s.s.[a]	−1.498(354)	10	0.69	10
Cu/Ni (Fe) – vacuum	−9.912(1507)	19855(2397)	−2.245(164)	14	0.97	$5032367e^{-0.00801547 * T(K)}$
Ge/Ni (FeS) – vacuum	*Highly volatile*[b]	–	–	–	–	–
Ge/Ni (FeS) – 1 bar	*Highly volatile*[b]	–	–	–	–	–
Ge/Ni (Fe) – vacuum	−9.574(2833)	20335(4507)	−2.768(308)	15	0.92	$447837e^{-0.00647200 * T(K)}$
Mo/Ni (FeS) – vacuum	−2.284(1054)	4676(1817)	−0.686(103)	9	0.87	$133086e^{-0.00600614 * T(K)}$
Ru/Ni (FeS) – vacuum	*Volatile*[c]	–	–	–	–	–
Ru/Ni (FeS) – 1 bar	*Volatile*[c]	–	–	–	–	–
Ag/Ni (FeS) – vacuum	−2.293(1407)	n.s.s.[a]	−1.407(320)	11	0.68	–
Ag/Ni (Fe) – vacuum	−9.538(3774)	11523(6034)	−0.907(399)	13	0.56	–
Ag/Ni (Fe) – 1 bar	−6.103(2869)	12845(4963)	−1.936(206)	14	0.90	–
W/Ni (FeS) – vacuum	*Volatile*[b]	–	–	–	–	–
W/Ni (FeS) – 1 bar	*Volatile*[b]	–	–	–	–	–
Re/Ni (FeS) – vacuum	*Volatile*[c]	–	–	–	–	–
Re/Ni (FeS) – 1 bar	*Volatile*[c]	–	–	–	–	–
Ir/Ni (FeS) – vacuum	*Volatile*[c]	–	–	–	–	–
Ir/Ni (FeS) – 1 bar	*Volatile*[c]	–	–	–	–	–
Excluding plateau values						
Cu/Ni (Fe) – vacuum	−10.484(1453)	20881(2255)	−2.275(204)	12	0.97	$5896697e^{-0.00808116 * T(K)}$
Ge/Ni (Fe) – vacuum	−8.408(3166)	19164(4780)	−3.166(432)	13	0.92	$65090e^{-0.00531401 * T(K)}$
Ag/Ni (FeS) – vacuum	−1.351(826)	n.s.s.[a]	−2.248(703)	8	0.63	–
Ag/Ni (Fe) – vacuum	−8.304(4056)	10560(6385)	−1.484(611)	11	0.59	–

[a] n.s.s. = not statistically significant. [b] due to high volatility samples were (almost) fully degassed at any pressure, temperature and time considered. [c] Assessment remains uncertain due to highly heterogeneous distribution in FeS matte as a result of their low solubility and resulting nugget formation.

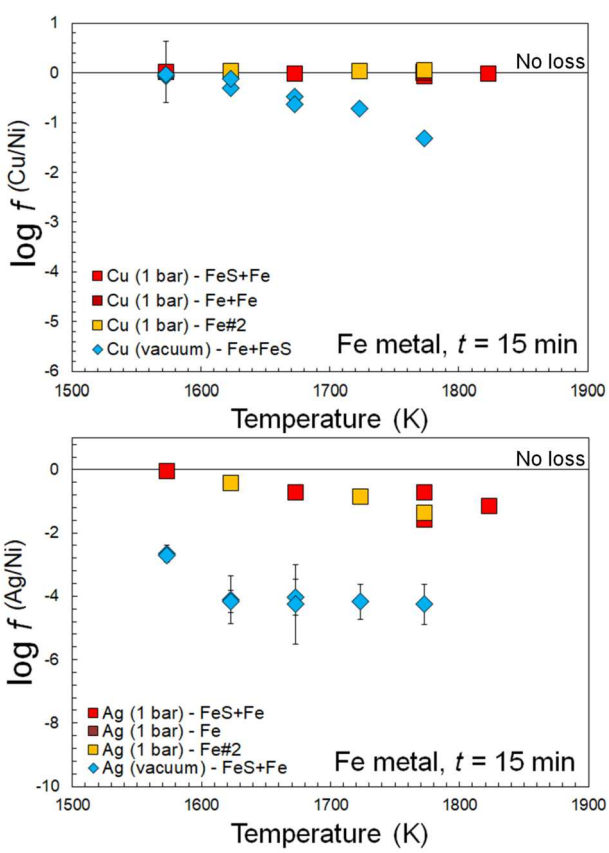

Fig. 4. Evaporative loss factors, normalized to Ni (Eq. (1), (2)), versus temperature, for Fe liquids. The time of 15 minutes represents the experimental run time, i.e., not incorporating lag time. See Fig. 3 caption for additional details.

free Fe liquid. Sulfur, Cu, Ge and Ag are carbon-avoiding (Siebert et al., 2011; Norris, 2017 and references therein) and therefore will likely behave relatively less volatile in C-free Fe liquid, relative to C-saturated Fe melt. Finally, it is expected that the effects of C in FeS liquid on elemental volatility are small or negligible, given the very low solubility of C in such melts (i.e., 0.2–0.3 wt.% C; e.g., Zhang et al., 2018).

3.4. Empirical parameterizations describing volatilities

Application of commonly used thermodynamic models to our data (e.g., Sossi et al., 2019) would require insights into the species that are evaporated, which in many cases are currently not or poorly constrained and/or could also involve multiple species depending on *P-T* conditions. We therefore obtained empirical parameterizations describing the volatilities of the elements of interest (S, Cu, Ge, Ag, Mo) as a function of experimental run time (t, in min) and temperature (*T*). The experimental data (Table S.4) were fitted to Eq. (3) using multiple linear regressions:

$$\log f^{(i/Ni)} = A + B\left(\frac{1}{T\,(K)}\right) + C\left(\log(\text{experimental run time}_{(min)})\right) \quad (3)$$

where *T* is temperature in K and *t* is time in minutes. Equation (3) was chosen to provide a reasonable predictor of the experimental data as a function of time and temperature. The experimental run time is different than the effective degassing time as a lag time may exist between heating and melting of the samples (e.g., Sossi et al., 2019). Pressure was also not included as a term in Eq. (3), as only two pressure anchor points are available to constrain the effects of pressure. Multiple linear regressions were performed separately for data obtained for FeS or Fe melts and for

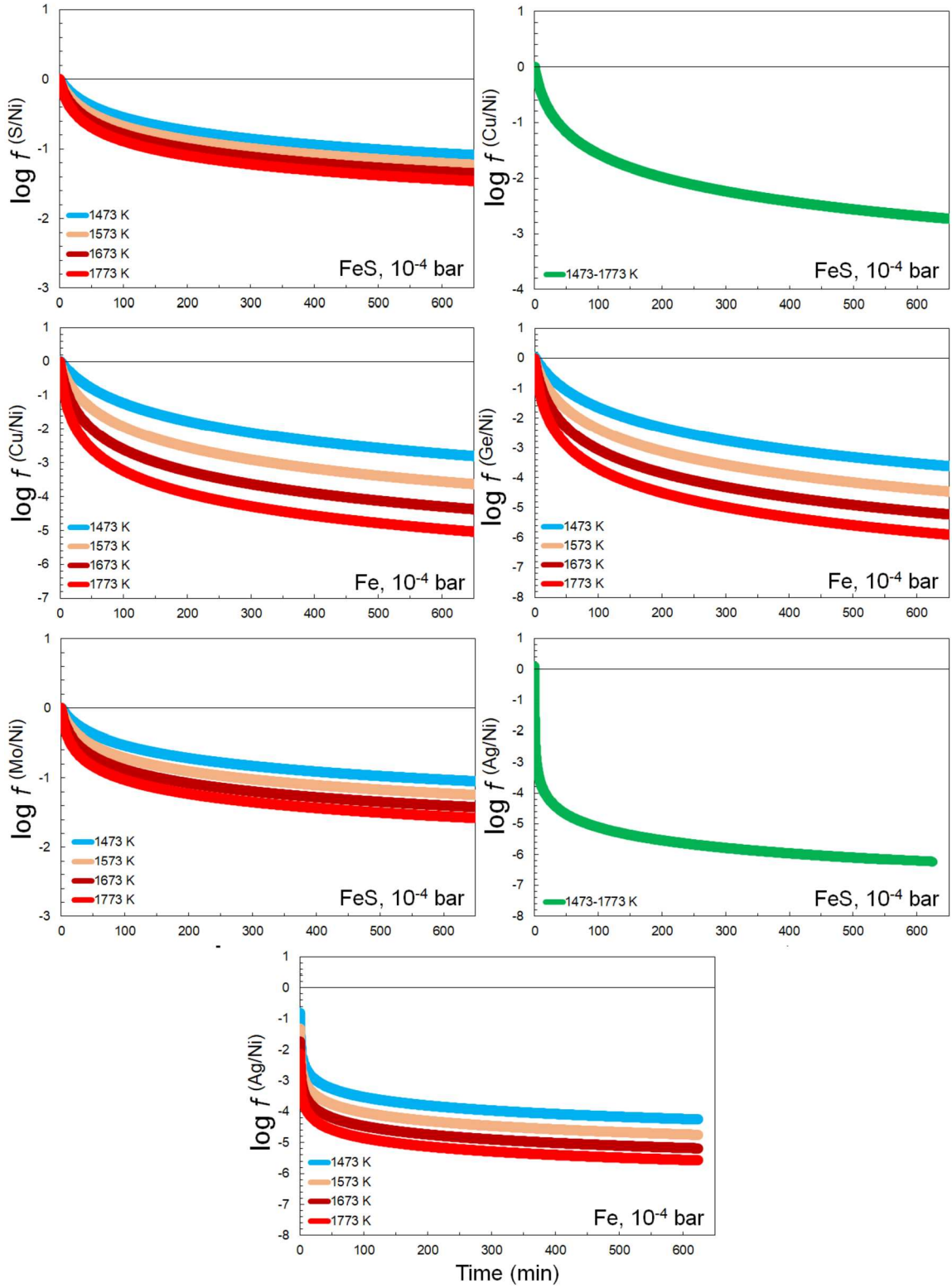

Fig. 5. Modeled Ni-normalized evaporative loss factors of the elements of interest (where available), calculated using Eq. (3) in conjunction with the fit parameters from Table 2, at 10^{-4} bar for FeS and/or Fe liquids, as a function of evaporation time. Green lines indicate modeled dependencies for which no temperature effects could be derived (see main text).

data obtained at vacuum or at 1 bar. Multiple linear regressions were performed using RegressIt©, an openly available Excel add-in package. Fit parameters were considered to be statistically significant if the Pearson correlation coefficient (p) is <0.10.

Table 2 provides a summary of the potential volatile behavior of the elements of interest and the derived fit parameters (where applicable) and Fig. 5 shows some of these results graphically. The lack of statistically significant parameters in Table 2 for some of the elements generally indicates that the volatility of the element of interest is little affected by the parameters considered. For Cu, Ge and Ag in FeS liquid, no temperature dependencies on their volatility could be constrained, independent of pressure. This is

Table 3
Derived reaction rate constants (k_i values) for the elements of interest for each set of temperature and pressure conditions. The y-axis intercept was forced to 0 with slope determination. The radius was assumed to be 0.15 cm in all cases.

	Composition	T (K)	Pressure	Time range (min)	k_i (cm/min)	Slope	1SE	R^2	N	Comment
S	FeS	1773	1 bar	5–120	6.00 x 10^{-5}	−1.20 x 10^{-3}	3.00 x 10^{-4}	0.78	6	All data
S	FeS	1673	vacuum	15–120	9.80 x 10^{-4}	−1.95 x 10^{-2}	1.80 x 10^{-3}	0.97	5	All data
S	FeS	1773	vacuum	5–60	3.66 x 10^{-3}	−7.31 x 10^{-2}	8.90 x 10^{-3}	0.97	3	All data
Cu	FeS	1673	vacuum	15–120	1.50 x 10^{-3}	−3.00 x 10^{-2}	8.10 x 10^{-3}	0.77	5	All data
Cu	FeS	1773	vacuum	5–60	3.93 x 10^{-3}	−7.85 x 10^{-2}	2.15 x 10^{-2}	0.87	3	All data
Cu	Fe	1673	vacuum	15–120	2.86 x 10^{-3}	−5.72 x 10^{-2}	3.80 x 10^{-3}	0.99	3	All data
Cu	Fe	1773	vacuum	5–120	3.39 x 10^{-3}	−6.77 x 10^{-2}	1.57 x 10^{-2}	0.82	5	All data
Cu	Fe	1773	vacuum	5–60	5.70 x 10^{-3}	−1.14 x 10^{-1}	1.94 x 10^{-2}	0.92	4	Excluded plateau value CRESS-40-Fe
Ge	FeS	1773	1 bar	–	–	–	–	–	–	Fitting not possible due to highly volatile behavior
Ge	FeS	1673	vacuum	–	–	–	–	–	–	Fitting not possible due to highly volatile behavior
Ge	FeS	1773	vacuum	–	–	–	–	–	–	Fitting not possible due to highly volatile behavior
Ge	Fe	1773	1 bar	5–90	1.35 x 10^{-4}	−2.70 x 10^{-3}	1.10 x 10^{-3}	0.42	10	All data
Ge	Fe	1673	vacuum	15–120	2.80 x 10^{-3}	−5.60 x 10^{-2}	4.30 x 10^{-3}	0.99	3	All data
Ge	Fe	1773	vacuum	5–120	4.08 x 10^{-3}	−8.16 x 10^{-2}	1.73 x 10^{-2}	0.85	5	All data
Ge	Fe	1773	vacuum	5–60	6.82 x 10^{-3}	−1.36 x 10^{-1}	1.67 x 10^{-2}	0.96	4	Excluded plateau value CRESS-40-Fe
Mo	FeS	1673	vacuum	15–120	7.05 x 10^{-4}	−1.41 x 10^{-2}	2.70 x 10^{-3}	0.87	5	All data
Mo	FeS	1773	vacuum	–	–	–	–	–	–	Fitting not possible due to lack of data; excluded CRESS-46
Ag	FeS	1673	vacuum	–	–	–	–	–	–	Fitting not possible due to highly volatile behavior
Ag	FeS	1773	vacuum	–	–	–	–	–	–	Fitting not possible due to highly volatile behavior
Ag	Fe	1773	1 bar	5–90	4.62 x 10^{-3}	−9.23 x 10^{-2}	1.08 x 10^{-2}	0.90	10	All data
Ag	Fe	1673	vacuum	15–120	2.86 x 10^{-3}	−5.72 x 10^{-2}	6.74 x 10^{-2}	0.50	3	All data
Ag	Fe	1773	vacuum	5–120	5.99 x 10^{-3}	−1.20 x 10^{-1}	4.42 x 10^{-2}	0.64	5	All data
Ag	Fe	1773	vacuum	5–60	1.12 x 10^{-2}	−2.23 x 10^{-1}	7.59 x 10^{-2}	0.74	4	Excluded plateau value CRESS-40-Fe

because they behave either too volatile (Ge, Ag) or insufficiently volatile (Cu) at these conditions (Fig. 3, 4). As previously discussed, no reliable fits could be obtained for Ru, W, Re and Ir, predominantly due to their heterogeneous distributions in the sulfide melts as nuggets, resulting in very large uncertainties of their derived bulk abundances (Fig. S.10, S.11, S.12 and Table S.2). We recommend that their potentially volatile behavior should be accurately constrained at very low initial concentrations (i.e., ppm levels) in a future study.

However, some parameterizations yield modeled log $f^{(i/Ni)}$ values that exceed 0 at short timescales. This is considered to reflect the "lag time" previously observed by Sossi et al. (2019), that depends on experimental arrangement, such as heating time and thermal conductivity of the starting material, the use of a powder instead of a solid starting material, the grain size and the overall size of the sample. We therefore added an element-specific lag-time parameter to each parameterization to account for this, which in turn also depends on temperature (i.e., higher temperature yields a shorter heating time required for melting of the sample):

$$\text{Effective degassing time } (t_d \text{ in min}) = \text{experimental run time } (t \text{ in min}) - \text{lag time } (t_0 \text{ in min}) \quad (4)$$

The actual experimental run time minus the lag time is defined as the "effective degassing time" or t_d (Eq. (4)). The lag time is determined for each element using the difference between the modeled log(i/Ni) value and 0 at the experimental run time of 0 at a given temperature. These results show that the lag time as a function of temperature is most accurately described using exponential fits (Fig. S.19) and that these vary between 0–17 min at 1573 and 2–5 min at 1823 K, depending on the element. We emphasize that the latter lag times are strictly only valid within the experimental temperature range, i.e., between 1573-1823 K, and cannot be extrapolated to lower temperatures.

We also calculated the reaction rate constant (k_i) of the evaporation of the elements of interest using a fully thermodynamic approach, while considering the radius (r) of the sample (0.15 cm), the time (t in min) and the natural logarithm of the ratio between the initial concentration (C_0) and the final concentration (C) (Tsuchiyama et al., 1981; Sossi et al., 2019, see Supplementary Information File section A.3; Table 3):

$$\ln(C/C_0) = -\frac{3k_i t}{r} \quad (5)$$

The slope was derived by consideration of $\ln(C/C_0)$ of each element versus time in minutes at a given pressure and temperature. The k_i values were then calculated by Eq. (6)

$$k_i = \frac{\text{slope} * r}{-3} \quad (6)$$

Table 3 lists the derived k_i values. As expected, k_i values increase with temperature and also vary significantly for FeS and Fe melt, as observed earlier in this study (Fig. S.20).

The plateau values observed for Cu, Ge and Ag for FeS and/or Fe liquid are potentially the result of the analytical difficulties of measuring their elemental abundances which are close to detection limits. However, it could also reflect a steady state between the furnace atmosphere and sample or (an)other process(es). The incorporation of these measurements in the parameterizations may result in erroneous results and therefore the data of Cu and Ge for Fe at vacuum and Ag for both Fe and FeS liquid at vacuum were also parameterized by excluding the aforementioned plateau values (Table 2). However, the results are near-identical, except for a slightly faster loss at a given temperature, pressure and composition. Finally, Table 2 shows that the fit for Ag in the Fe system at 1 bar, based on values that far exceed the detection limit, is near-identical to the fit for Ag in the same system at high vacuum. Therefore, we conclude that the parameterizations and corresponding lag times that were obtained in the earlier section are robust

throughout the experimental range and are not significantly affected by the incorporation of plateau values.

4. Discussion

4.1. Comparison with currently applied volatility models

The 50% condensation temperatures (Lodders, 2003; Wood et al., 2019) are often used as a proxy for elemental volatility for a wide range of planetary processes (e.g., Wai and Wasson, 1979; Campbell and Humayun, 2005). However, the nebular gas under which condensation occurred was highly reducing (ΔIW $= -7$; Wood et al., 2019), which is likely not relevant to evaporation from the large majority of metal-rich molten planetesimals. Soon after dissipation of the primordial H-rich atmosphere, silicate/metal-gas equilibria would instead be governed by the Fe-FeO equilibrium, yielding much more oxidized conditions (i.e., ΔIW -1 to -2.5; Righter et al., 1998; Wood et al., 2006). This large difference in redox state could significantly affect the predicted volatility of the elements of interest. Indeed, the relevant volatility sequence predicted by the condensation temperature models would be S, Ag $<$ Ge $<$ Cu $<$ Mo, Ru $<$ Re, W, over a range of ~700 to 1740 K at 0.0001 bar (Wood et al., 2019). At these pressures, our experimental results for Fe liquid suggests a similar sequence, i.e., Ag $<$ Ge $<$ Cu, while Cr, Co, Mo, Pd Ru, Re, W were found to be not volatile. However, this is significantly different for FeS liquid, where volatility increases in the order of Ge, Ag $<$ Cu $<$ S, Mo, Ru, W, Re, Ir $<$ Cr, Co, Pd. The presence of S thus significantly affects their volatility which agrees with previous experimental and thermodynamic studies that found major effects of silicate melt and gas-phase composition on evaporation behavior (e.g., Renggli and Klemme, 2020; Pangritz et al., 2022). The comparison also clearly shows that 50% condensation temperatures are not directly applicable to evaporation processes on metal-rich planetesimals.

4.2. Evaporative loss from the IVB parent body?

We now demonstrate the applicability of our experimental data and the new parameterizations to assess potential evaporative loss from the IVB parent body, which is the source of the IVB iron meteorites, the most volatile element-depleted magmatic iron meteorite suite. The volatile element contents of the IVB iron meteorites cannot be directly used as bulk parent body concentrations, as the suite has experienced extensive magmatic differentiation (up to 86% of metal crystallization), as evidenced from major, minor and trace element systematics (e.g., Campbell and Humayun, 2005; Zhang et al., 2022). We therefore used reconstructed IVB parent melt compositions (Chabot, 2004 for S; Campbell and Humayun, 2005 for all other elements) in conjunction with a CI chondritic bulk composition (taken from Alexander, 2019) to obtain volatile element depletion factors of the elements of interest (Table S.1). It should be noted that no uncertainties are reported for these estimates in the latter studies. No estimates for Ag for IVB parent melt compositions are currently available. We therefore assumed the average of two reported parent body melt concentrations for Muonionalusta (1 and 3 ppb, respectively), a group IVA iron meteorite, from Horan et al. (2012) (Table 2). Finally, Mo isotopes have also been used to infer a carbonaceous chondritic heritage of the IVB parent body (Budde et al., 2016), justifying our choice of the IVB parent body bulk composition.

We assumed a 10% uncertainty on previously published parental melt and bulk CI concentrations as no uncertainties were reported in the latter studies. Finally, the assumed metallic parental melt composition does not include the silicate portion of the IVB parent body (Campbell and Humayun, 2005). However, taking the reasonable assumption that equilibrium was (largely) achieved between

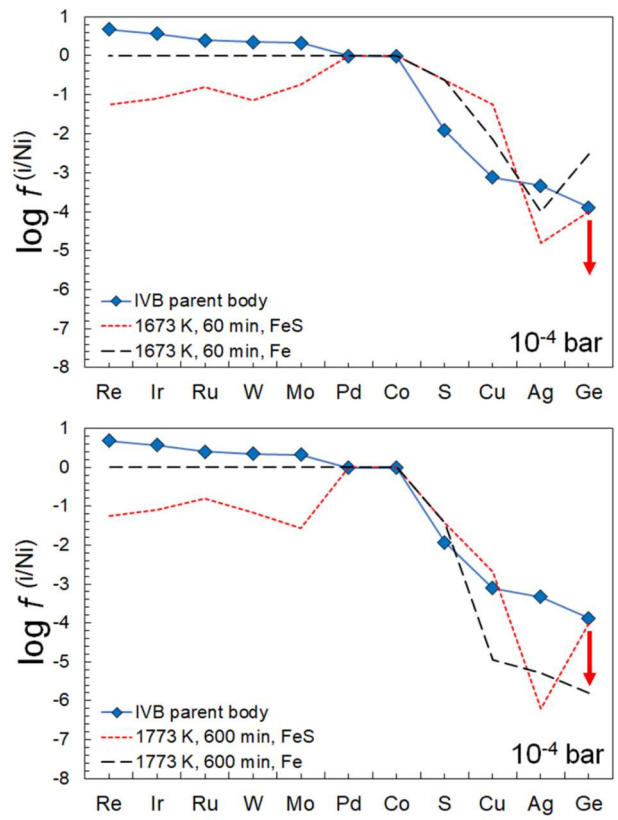

Fig. 6. Comparison between modeled Ni-normalized evaporative loss factors of the elements of interest, calculated using Eq. (3) in conjunction with the fit parameters from Table 2 for FeS and/or Fe liquids while incorporating the plateau values, and evaporative loss factors required for explaining reconstructed IVB bulk parent body depletions. Note that Chabot (2004) and Campbell and Humayun (2005) do not report uncertainties on these estimates. Modeling results were obtained at 1673 or 1773 K, evaporation time of 60 and 600 min, all at 10^{-4} bar. The evaporation behavior of S was assumed to be identical for FeS and Fe liquids. Evaporative loss factors for Ru, W, Re Ir were estimated from experimental results obtained at the modeled time and temperature. The red arrow indicates that Ge is potentially more depleted in the experimental samples as Ge contents are often close to the detection limit of 0.1 to 0.2 ppm (Supplementary Table S.1).

the metallic and silicate fractions, all of the elements considered in our model should have partitioned almost completely into the metallic phase (S, Cu, Ge, Mo, Ag), given their moderately to highly siderophile behavior at the estimated redox state of IVB parent body differentiation (ΔIW $= -1$; Campbell and Humayun, 2005; Steenstra et al., 2017).

The required evaporative loss factors to explain the depletions in the IVB magmatic iron meteorites solely by evaporation were then calculated using Eq. (2) and the previously discussed bulk estimates, and are listed in Table S.4. To assess the likelihood of evaporative loss from a metallic liquid being a major contributor to volatile loss in the IVB parent body, we compared the modeled evaporative loss factors for FeS and Fe at 10^{-4} bar with the required evaporative loss factors for the IVB parent body. This hypothesis assumes that the IVB parent body core was exposed to space for some time. An important first observation is that volatility trends for nominally volatile elements (S, Cu, Ge, Ag) are reasonably reproduced by all of the modeled scenarios (Fig. 6). However, it is also clear that evaporation of a S-rich melt would certainly result in a significant depletion of Mo, Ru, W, Re and Ir, which is not observed for the IVB parent body, where these elements are actually enriched instead of depleted relative to CI chondrite (Fig. 6). This is a robust conclusion for Mo and to a lesser extent Ru, W, Re and Ir, despite major uncertainties in the exact magnitude of their depletion in experimental samples. Based on

these results alone, it can therefore be concluded that evaporation on the IVB parent body could only have occurred under relatively S-poor conditions. Results for the Fe melt, however, demonstrate how feasible evaporation processes are in explaining the depletions of the elements of interest in the IVB parent body (Fig. 6). Our results are therefore consistent with evaporation of an exposed, molten IVB parent body core, as a result of (a) large impact(s). As proposed by Matthes et al. (2018), for the IVA parent body, evaporation of Ag is generally an attractive model for explaining the Pd-Ag isotope systematics of these samples as it strongly depletes Ag and provides a late Pd/Ag fractionation, after which the cores would have rapidly cooled. However, as noted by Matthes et al. (2018), there are some geochemical observations that may not be consistent with (solely) evaporative loss from the IVB parent body core. The reconstructed pre-exposure δ^{65}Cu data for the IVB suite are slightly negative (Chen et al., 2016), which is the opposite of what would be expected if Cu was predominantly lost through evaporation (Bishop et al., 2012; Chen et al., 2016). Alternatively, Cu could have been extensively evaporated, followed by partial recondensation of Cu in the kinetic regime, yielding a final light δ^{65}Cu value for the IVB parent body. This mechanism has been proposed for reconciling the light δ^{41}K isotopic composition of angrites with the extreme elemental depletion of K in angrites (Hu et al., 2022).

It should also be noted that it is unlikely that the IVB parent body experienced graphite saturation given extensive C loss (e.g., Hirschmann et al., 2021 and references therein) and the derived evaporative loss factors for Fe-rich melt are likely affected by carbon saturation in our experiments. The possibility can also not be excluded that evaporation of the elements of interest occurred from the silicate melt covering the core, where the present-day IVB meteorite volatile element depletion signature would simply reflect the partitioning of these highly depleted elements from the silicate mantle to the core. Alternatively, incomplete nebular condensation may account for the depletions of (some) of the elements of interest. Future work should thus include the evaporation systematics of more volatile and highly volatile elements, with which the potential importance of evaporative loss can be studied in greater detail using multi-element solutions. Finally, the effects of C on evaporative loss from metallic melts needs to be experimentally tested and constrained.

5. Conclusions

The volatility of a suite of siderophile elements was experimentally assessed under vacuum and room pressures for Fe and FeS melts. Elements S, Fe, Cu, Ge, Ag, Mo, W and likely Ru, W, Ir were found to evaporate at 1573–1823 K, the depletion depending on *P-T*, composition and duration. Composition of the core-forming liquid strongly affects volatility, with the volatility of Ge, Mo, Ru, W, Re and Ir being strongly increased through the presence of S and Cu and Ag were found to behave less volatile in the presence of S. These results demonstrate the importance of melt composition for evaporation systematics. Application of the new thermodynamic parameterizations to IVB parent body depletions shows that the latter can be easily explained through evaporation of a S-free or S-poor Fe liquid core under a wider range of temperatures and evaporation durations. Our results are therefore consistent with a potentially important role of evaporative loss on establishing the volatile element depletions in the IVB parent body.

CRediT authorship contribution statement

E.S. Steenstra: Writing – original draft, Methodology, Investigation, Funding acquisition, Formal analysis, Data curation, Conceptualization. **C.J. Renggli:** Writing – review & editing, Methodology, Investigation, Funding acquisition, Data curation, Conceptualization. **J. Berndt:** Writing – review & editing, Funding acquisition, Formal analysis. **S. Klemme:** Writing – review & editing, Supervision, Resources, Project administration, Funding acquisition.

Declaration of competing interest

The authors declare that they have no known competing financial interests or personal relationships that could have appeared to influence the work reported in this paper.

Data availability

Data will be made available on request.

Acknowledgements

We thank Maik Trogisch and Beate Schmitte for their excellent sample preparation and assistance with EPMA and LA-ICP-MS analyses, respectively. We also would like to thank Paolo Sossi, an anonymous reviewer and the editor for useful comments that greatly improved the manuscript. This study was funded by SFB TRR-170 and a Marie Curie Postdoctoral Fellowship to E.S.S.; C.R. was funded by the Deutsche Forschungsgemeinschaft (DFG, German Research Foundation) – project 442083018. This is TRR-170 publication no. **204**.

Appendix A. Supplementary material

Supplementary material related to this article can be found online at https://doi.org/10.1016/j.epsl.2023.118406.

References

Alexander, C.M.O'D., 2019. Quantitative models for the elemental and isotopic fractionations in chondrites: the carbonaceous chondrites. Geochim. Cosmochim. Acta 254, 277–309.
Bishop, M.C., Moynier, F., Weinstein, C., Fraboulet, J.-G., Wang, K., Foriel, J., 2012. The Cu isotopic composition of iron meteorites. Meteorit. Planet. Sci. 47 (2), 268–276.
Budde, G., Burkhardt, C., Brennecka, G.A., Fischer-Goedde, M., Kruijer, T.S., Kleine, T., 2016. Molybdenum isotopic evidence for the origin of chondrules and a distinct heritage of carbonaceous and non-carbonaceous meteorites. Earth Planet. Sci. Lett. 454, 293–303.
Buono, A.S., Walker, D., 2011. The Fe-rich liquidus in the Fe-FeS system from 1 bar to 10 GPa. Geochim. Cosmochim. Acta 75, 2072–2087.
Campbell, A.J., Humayun, M., 2005. Compositions of group IVB iron meteorites and their parent melt. Geochim. Cosmochim. Acta 69 (19), 4733–4744.
Chabot, N.L., 2004. Sulfur contents of the parental metallic cores of magmatic iron meteorites. Geochim. Cosmochim. Acta 68, 3607–3618.
Chabot, N.L., Zhang, B., 2021. A revised trap melt model for iron meteorites applied to the IIIAB group. Meteorit. Planet. Sci. 1 (28). https://doi.org/10.1111/maps.13740.
Chen, H., Nguyen, B.M., Moynier, F., 2013. Zinc isotopic composition of iron meteorites: absence of isotopic anomalies and the origin of the volatile element depletion. Meteorit. Planet. Sci. 48, 2441–2450.
Chen, H., Moynier, F., Humayun, M., Cole Bishop, M., Williams, J.T., 2016. Cosmogenic effects on Cu isotopes in IVB iron meteorites. Geochim. Cosmochim. Acta 182, 145–154.
Corgne, A., Wood, B.J., Fei, Y., 2008. C- and S-rich molten alloy immiscibility and core formation of planetesimals. Geochim. Cosmochim. Acta 72, 2409–2416.
Davis, A.M., 2006. Volatile evolution and loss. In: Lauretta, D.S., McSween Jr., H.Y. (Eds.), Meteorites and the Early Solar System II. University of Arizona Press, Tucson, pp. 295–307.
Fonseca, R.O.C., Mallmann, G., O'Neill, H.St.C., Campbell, I.H., 2007. How chalcophile is rhenium? An experimental study of the solubility of Re in sulphide mattes. Earth Planet. Sci. Lett. 260, 537–548.
Fonseca, R.O.C., Mallmann, G., O'Neill, H.St.C., Campbell, I.A., Laurenz, V., 2011. Solubility of Os and Ir in sulfide melt: Implications for Re/Os fractionation during mantle melting. Earth Planet. Sci. Lett. 311, 339–350.
Gargano, A., Sharp, Z., 2019. The chlorine isotope composition of iron meteorites: evidence for the Cl isotope composition of the solar nebula and implications for extensive devolatilization during planet formation. Meteorit. Planet. Sci. 54, 1619–1631.

Goldstein, J.I., Scott, E.R.D., Chabot, N.L., 2009. Iron meteorites: crystallization, thermal history, parent bodies, and origin. Chem. Erde 69, 293–325.
Griffin, W.L., Powell, W.J., Pearson, N.J., O'Reilly, S.Y., 2008. GLITTER: data reduction software for laser ablation ICP-MS. In: Sylvester, P. (Ed.), Laser Ablation ICPMS in the Earth Sciences: Current Practices and Outstanding Issues. In: Mineralogical Association of Canada. Short Course Series, vol. 40, pp. 308–311.
Hirschmann, M.M., Bergin, E.A., Blake, G.A., Ciesla, F.J., Li, J., 2021. Early volatile depletion on planetesimals inferred from C-S systematics of iron meteorite parent bodies. Proc. Natl. Acad. Sci. 118 (13), e2026779118.
Horan, M.F., Carlson, R.W., Blichert-Toft, J., 2012. Pd-Ag chronology of volatile depletion, crystallization and shock in the Muonionalusta IVA iron meteorite and implications for its parent body. Earth Planet. Sci. Lett. 351–352, 215–222.
Hu, Y., Moynier, F., Bizzarro, M., 2022. Potassium isotope heterogeneity in the early Solar System controlled by extensive evaporation and partial recondensation.
Jochum, K.P., Nohl, U., Herwig, K., Lammel, E., Stoll, B., Hofmann, A.W., 2005a. GeoReM: a new geochemical database for reference materials and isotopic standards. Geostand. Geoanal. Res. 29, 333–338.
Jochum, K.P., Willbold, M., Raczek, I., Stoll, B., Herwig, K., 2005b. Chemical characterization of the USGS reference glasses GSA-1G, GSC-1G, GSD-1G, GSE937 1G, BCR-2G, BHVO-2G and BIR-1G using EPMA, ID-TIMS, ID-ICPMS and LA938 ICPMS. Geostand. Geoanal. Res. 29, 285–302.
Kleine, T., Matthes, M., Nimmo, F., Leya, I., 2018. Silver isotopic evidence for impact-driven volatile loss from differentiated asteroids. In: LPSC 49, p. 2083 (abstr.).
Kruijer, T.S., Burkhardt, C., Budde, G., Kleine, T., 2017. Age of Jupiter inferred from the distinct genetics and formation times of meteorites. Proc. Natl. Acad. Sci. 114 (26), 6712–6716.
Lodders, K., 2003. Solar system abundances and condensation temperatures of the elements. Astrophys. J. 591, 1220.
Lord, O.T., Walter, M.J., Dasgupta, R., Walker, D., Clark, S.M., 2009. Melting in the Fe-C system to 70 GPa. Earth Planet. Sci. Lett. 284, 157–167.
Luck, J.M., Othman, D.B., Barrat, J.A., Albarède, F., 2003. Coupled ^{63}Cu and ^{16}O excesses in chondrites. Geochim. Cosmochim. Acta 67, 143–151.
Luck, J.M., Othman, D.B., Albarède, F., 2005. Zn and Cu isotopic variations in chondrites and iron meteorites: early solar nebula reservoirs and parent-body processes. Geochim. Cosmochim. Acta 69, 5351–5363.
Matthes, M., Fischer-Gödde, M., Kruijer, T.S., Kleine, T., 2018. Pd-Ag chronometry of IVA iron meteorites and the crystallization and cooling of a protoplanetary core. Geochim. Cosmochim. Acta 220, 82–95.
Norris, A., 2017. The metal activity calculator. Acces via: https://norris.org.au/expet/metalact/.
Pangritz, P., Renggli, C.J., Berndt, J., Rohrbach, A., Klemme, S., 2022. Influence of S and Cl on the evaporation of Cu from silicate melts. In: Goldschmidt 2022 (abstr.).
Rasmussen, K.L., Malvin, D.J., Buchwald, V.F., Wasson, J.T., 1984. Compositional trends and cooling rates of group IVB iron meteorites. Geochim. Cosmochim. Acta 48, 805–813.
Renggli, C.J., Klemme, S., 2020. Experimental constraints on metal transport in fumarolic gases. J. Volcanol. Geotherm. 400, 106929.
Richter, F.M., Mendybaev, R.A., Christensen, J.N., Ebel, D., Gaffney, A., 2011. Laboratory experiments bearing on the origin and evolution of olivine-rich chondrules. Meteorit. Planet. Sci. 46 (8), 1152–1178.
Righter, K., Hervig, R.L., Kring, D.A., 1998. Accretion and core formation on Mars: molybdenum contents of melt inclusion glasses in three SNC meteorites. Geochim. Cosmochim. Acta 62, 2167–2177.
Rubin, A.E., 2018. Carbonaceous and noncarbonaceous iron meteorites: differences in chemical, physical, and collective properties. Meteorit. Planet. Sci. 53 (11), 2357–2371.
Scott, E.R.D., Wasson, J.T., 1975. Classification and properties of iron meteorites. Rev. Geophys. 13, 527–546.
Scott, E.R.D., 1978. Tungsten in iron meteorites. Earth Planet. Sci. Lett. 39, 363–370.
Scott, E.R.D., 1979. Origin of anomalous iron meteorites. Mineral. Mag. 43, 415–421.
Swartzendruber, L.J., 1984. The Ag-Fe (Silver-Iron) system. Bull. Alloy Phase Diagr. 5, 560–564.
Sears, D.W., 1978. Condensation and the composition of iron meteorites. Earth Planet. Sci. Lett. 41, 128–138.
Siebert, J., Corgne, A., Ryerson, F.J., 2011. Systematics of metal-silicate partitioning for many siderophile elements applied to Earth's core formation. Geochim. Cosmochim. Acta 75, 1451–1489.
Sossi, P.A., Klemme, S., O'Neill, H.St.C., Berndt, J., Moynier, F., 2019. Evaporation of moderately volatile elements from silicate melts: experiments and theory. Geochim. Cosmochim. Acta 260, 204–231.
Sossi, P.A., Moynier, F., Treilles, R., Mokhtari, M., Wang, X., Siebert, J., 2020. An experimentally-determined general formalism for evaporation and isotope fractionation of Cu and Zn from silicate melts between 1300 and 1500 C and 1 bar. Geochim. Cosmochim. Acta 288, 316–340.
Steenstra, E.S., Sitabi, A.B., Lin, Y.H., Rai, N., Knibbe, J.S., Berndt, J., Matveev, S., van Westrenen, W., 2017. The effect of melt composition on metal-silicate partitioning of siderophile elements and constraints on core formation in the angrite parent body. Geochim. Cosmochim. Acta 212, 62–83.
Steenstra, E.S., Berndt, J., Klemme, S., van Westrenen, W., 2019. LA-ICP-MS analyses of Fe-rich alloys: quantification of matrix effects for 193 nm excimer laser systems. J. Anal. At. Spectrom. 34, 222–231.
Steenstra, E.S., Berndt, J., Klemme, S., van Westrenen, W., Bullock, E.S., Shahar, A., 2020. Addressing matrix effects for 193 nm excimer LA-ICP-MS analyses of Fe-rich sulfides and a new predictive model. J. Anal. At. Spectrom. https://doi.org/10.1039/C9JA00391F.
Tsuchiyama, A., Nagahara, H., Kushiro, I., 1981. Volatilization of sodium from silicate melt spheres and its application to the formation of chondrules. Geochim. Cosmochim. Acta 45, 1357–1367.
van Achterbergh, E., Ryan, C.G., Jackson, S.E., Griffin, W.L., 2001. Data reduction software for LA-ICP-MS: appendix. In: Sylvester, P.J. (Ed.), Laser Ablation-ICP Mass Spectrometry in the Earth Sciences: Principles and Applications. Ottawa: Mineralog. Assoc. Canada. In: Short Course Series, vol. 29. Mineralog. Assoc. Canada (MAC), Ottawa, pp. 239–243.
Wai, C.M., Wasson, J.T., 1979. Nebular condensation of Ga, Ge and Sb and the chemical classification of iron meteorites. Nature 282, 790–793.
Wohlgemuth-Ueberwasser, C.C., Ballhaus, C., Berndt, J., Paliulionyte, V.S., Meisel, T., 2007. Synthesis of PGE sulfide standards for laser ablation inductively coupled plasma mass spectrometry. Contrib. Mineral. Petrol. 154, 607–617.
Wood, B.J., Walter, M.J., Wade, J., 2006. Accretion of the Earth and segregation of its core. Nature 441, 825–833.
Wood, B.J., Kiseeva, E.S., Mirolo, F.J., 2014. Accretion and core formation: the effects of sulfur on metal-silicate partition coefficients.
Wood, B.J., Smythe, D.J., Harrison, T., 2019. The condensation temperatures of the elements: a reappraisal. Am. Mineral. 104 (6), 844–856.
Zhang, Z., Hastings, P., Von der Handt, A., Hirschmann, M.M., 2018. Experimental determination of carbon solubility in Fe-Ni-S melts. Geochim. Cosmochim. Acta 225, 66–79.
Zhang, B., Chabot, N.L., Rubin, A.E., 2022. Compositions of carbonaceous-type asteroidal cores in the early solar system. Sci. Adv. 8, eabo5781.

XMLVIEW: extended

Appendix A. Supplementary material

The following is the Supplementary material related to this article.

begin ecomponent begin ecomponent begin ecomponent begin ecomponent begin ecomponent begin ecomponent begin ecomponent begin ecomponent begin ecomponent begin ecomponent begin ecomponent begin ecomponent begin ecomponent begin ecomponent begin ecomponent begin ecomponent begin ecomponent

`Label:` MMC 1

`caption:` This document provides a summary of the chemical compositions of the various samples and the evaporative loss factors of the different elements. It also provides a detailed description of experimental and analytical details, as well as of the thermodynamic approach used to calculate reaction rate constants.

`link:` **APPLICATION : mmc1**

end ecomponent end ecomponent

begin ecomponent begin ecomponent begin ecomponent begin ecomponent begin ecomponent begin ecomponent begin ecomponent begin ecomponent begin ecomponent begin ecomponent begin ecomponent begin ecomponent begin ecomponent begin ecomponent begin ecomponent begin ecomponent begin ecomponent

`Label:` MMC 2

`caption:` This table summarizes all the raw and processed chemical data for each sample, as well as the reaction rate constants.

`link:` **APPLICATION : mmc2**

end ecomponent end ecomponent

Sponsor names

Do not correct this page. Please mark corrections to sponsor names and grant numbers in the main text.

Deutsche Forschungsgemeinschaft, *country*=Germany, *grants*=442083018

Highlights

- First experimental data of volatile element evaporation from metallic melts.
- Sulfur strongly affects elemental evaporation behavior.
- Volatile element depletions of IVB magmatic iron meteorites can be explained by evaporation.